

# Structural Organization and Transport Properties of Novel Pyrrolidinium-Based Ionic Liquids with Perfluoroalkyl Sulfonylimide Anions

Franca Castiglione,<sup>†</sup> Margherita Moreno,<sup>†</sup> Guido Raos,<sup>\*,†</sup> Antonino Famulari,<sup>†</sup> Andrea Mele,<sup>\*,†</sup> Giovanni Battista Appetecchi,<sup>‡</sup> and Stefano Passerini<sup>\*,§</sup>

Dipartimento di Chimica, Materiali e Ingegneria Chimica “G. Natta”, Politecnico di Milano, Via L. Mancinelli 7, 20131 Milano, Italy, ENEA, Italian Agency for the New Technology, Energy, and the Environment, TER Dept., Via Anguillarese 301, Rome 00123, Italy, and Institute of Physical Chemistry, University of Muenster, Corrensstr. 28/30, D48149 Münster, Germany

Received: December 26, 2008; Revised Manuscript Received: June 29, 2009

Room-temperature ionic liquids (RTILs) based on the *N*-butyl-*N*-methyl pyrrolidinium cation (PYR<sub>14</sub><sup>+</sup>) combined with three different fluorinated anions have been prepared and characterized by NMR, conductivity, and rheological measurements. The anions are (trifluoromethanesulfonyl)(nonafluorobutanesulfonyl)imide (IM<sub>14</sub><sup>−</sup>), bis(pentafluoroethanesulfonyl)imide (BETI<sup>−</sup>), and bis(trifluoromethanesulfonyl)imide (TFSI<sup>−</sup>). Intermolecular anion–cation nuclear Overhauser enhancements (NOEs) have been experimentally observed in all titled compounds. These findings indicate the formation of long-lived aggregates in the bulk liquids. The NOE patterns show marked selectivity and can be rationalized assuming that the perfluorinated moieties of the anions tend to adopt a preferential orientation with respect to the cations, with possible formation of mesoscopic fluorine domains. Self-diffusion coefficients *D* for the anion and the cation have been measured by DOSY NMR. Diffusion data show similar but not identical values for cation and anion, consistent with local ordering at the molecular level. The observed trend in diffusion coefficients, *D*<sub>cation</sub> > *D*<sub>anion</sub> for all compounds, is compatible with a higher degree of intermolecular organization of the anions. This nanoscale organization is connected to rather strong deviations of the experimental conductivities from those estimated from the ion diffusion coefficients through the Nernst–Einstein relationship. The measured viscosities and ion diffusion coefficients in PYR<sub>14</sub>IM<sub>14</sub> and in PYR<sub>14</sub>TFSI have similar temperature dependencies, leading to very close values of the activation energies for these processes. Ab initio density functional calculations on models of a PYR<sub>14</sub>TFSI ion pair lead to the identification of several local minima, whose structure and energy can be qualitatively related to the experimental NOE signals and activation energies.

## 1. Introduction

Hydrophobic, air-stable room-temperature ionic liquids (RTILs) are being incorporated as electrolyte materials into a wide variety of electrochemical devices including lithium batteries,<sup>1–12</sup> electrochemical (super or ultra) capacitors,<sup>13–15</sup> electrochemical actuators,<sup>16–18</sup> light-emitting electrochemical cells,<sup>19–21</sup> etc. Such electrochemical applications have stringent requirements including high ionic conductivity, high chemical, thermal, and electrochemical stability, and wide liquid range for operation at low and high temperatures. When a lithium salt is added to a RTIL, the Li<sup>+</sup> conductivity is generally found to scale with the conductivity of the solvent. It was recently demonstrated that the combined use of *N*-propyl-*N*-methyl pyrrolidinium bis(trifluoromethanesulfonyl)imide ionic liquid (PYR<sub>13</sub>TFSI) with poly(ethyleneoxide) (PEO) LiTFSI polymer electrolytes significantly enhanced the ionic conductivity, compared to that of reference RTIL-free PEO electrolytes. Consequently, the performance of the corresponding Li ion battery significantly improved.<sup>22</sup> Thus, the coupling of pyrrolidinium-based RTILs

with conventional polymer electrolytes may provide an innovative medium for devices able to compete with established technology.

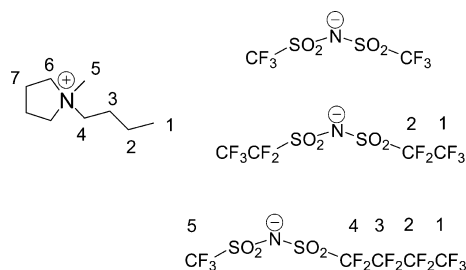
In view of coming-up applications of pyrrolidinium-based RTILs in electrochemical devices, a detailed knowledge of the network of interactions in the bulk liquid is required for a better understanding of physical properties such as ion conductivity. For example, Borodin et al.<sup>23</sup> showed—using molecular dynamics (MD) simulations with a suitably developed force field—that the transport properties and mechanisms of Li<sup>+</sup> dissolved in *N,N*-dialkyl pyrrolidinium TFSI ionic liquids are affected by the coordination of the metal ion with the anion of RTIL and by the ability of the latter to undergo exchange processes within the coordination shell. As a general remark, many important physicochemical properties—conductivity and viscosity among them—are strongly affected by the association and ordering of the ions in the liquid phase. The concept of “local structure” is largely used in the field of RTIL chemistry, and it is related to the fact that RTILs show short-range aggregation motives resembling, in some cases, those found in the solid state by single crystal X-ray diffraction studies. The resultant mesoscopic ordering is one of the most peculiar and fascinating features of RTILs, which has stimulated a number of physicochemical studies. A critical debate on general models for understanding RTIL properties at the molecular level is currently under way.<sup>24</sup>

\* To whom correspondence should be addressed. E-mail: guido.raos@polimi.it (G.R.); andrea.mele@polimi.it (A.M.).

<sup>†</sup> Politecnico di Milano.

<sup>‡</sup> Italian Agency for the New Technology, Energy, and the Environment.

<sup>§</sup> University of Muenster.

**SCHEME 1: Molecular Formula and Atom Numbering of PYR<sub>14</sub>TFSI (1), PYR<sub>14</sub>BETI (2), and PYR<sub>14</sub>IM<sub>14</sub> (3)<sup>a</sup>**

<sup>a</sup> Left: PYR<sub>14</sub><sup>+</sup> cation. Right: TFSI<sup>−</sup> (top), BETI<sup>−</sup> (middle), and IM<sub>14</sub><sup>−</sup> (bottom) anions.

In this scenario, we present a physicochemical characterization of three RTILs based on the same cation and different anions from the (perfluoroalkylsulfonyl)imide family (see Scheme 1). We bring together in a critical discussion the results from different experimental techniques, including NMR-based characterizations of the liquid structure and ion diffusion, rheological, and conductivity measurements. Special emphasis is devoted to accumulating experimental data on the aggregation motives, if any, of the perfluorinated anions, as they are expected to affect the Li<sup>+</sup> transport properties of the corresponding LiTFSI doped RTILs (vide supra). Finally, molecular modeling simulations are also presented. Following the approach of other authors,<sup>25,26</sup> we try to extract relevant pieces of information from quantum-chemical calculations on isolated gas-phase ion pairs.

## 2. Experimental and Computational Methods

**Materials.** The PYR<sub>14</sub>TFSI (1), PYR<sub>14</sub>BETI (2), and PYR<sub>14</sub>IM<sub>14</sub> (3) ionic liquids were synthesized through a novel procedure developed at ENEA and described in detail elsewhere.<sup>27</sup> The chemicals *N*-methylpyrrolidine (97 wt %), 1-bromobutane (99 wt %), and ethyl acetate (ACS grade, >99.5 wt %) were purchased from Aldrich and previously purified (with the exception of ethyl acetate) through activated carbon (Aldrich, Darco-G60) and alumina (acidic, Aldrich Brockmann I). Lithium bis(trifluoromethanesulfonyl)imide, LiTFSI (99.9 wt %, battery grade), lithium bis(pentafluoroethanesulfonyl)imide, LiBETI (99.9 wt %, battery grade), and acidic (trifluoromethanesulfonyl)(nonafluorobutylsulfonyl)imide, HIM<sub>14</sub> (59 wt % solution in water), were purchased by 3M and used as received. Deionized H<sub>2</sub>O was obtained with a Millipore ion-exchange resin deionizer.

The *N*-butyl-*N*-methylpyrrolidinium bromide, PYR<sub>14</sub>Br, precursor was synthesized by reacting *N*-methylpyrrolidine with the appropriate amount of bromobutane in the presence of ethyl acetate. The precursor was repeatedly rinsed with ethyl acetate to remove the reagent excess and the soluble impurities. The PYR<sub>14</sub>IM<sub>14</sub>, PYR<sub>14</sub>BETI, and PYR<sub>14</sub>TFSI ionic liquids were obtained by reacting aqueous solutions of PYR<sub>14</sub>Br precursor with the appropriate amount of LiTFSI, LiBETI, or HIM<sub>14</sub>. The reactions led to the formation of the hydrophobic ionic liquid and hydrophilic LiBr or HBr. After removal of the aqueous phase, the ionic liquids were rinsed several times with deionized water to remove water-soluble LiBr or HBr and the excess of LiTFSI, LiBETI, or HIM<sub>14</sub>. The ionic liquids were then purified with activated carbon and acidic alumina. The liquid fractions were separated from the solid phases by vacuum filtering and then placed in a rotary evaporator at 80 °C under a vacuum to remove the solvent (ethyl acetate). Finally, the ionic liquids were dried with an oil-free vacuum pump at 60 °C for at least 2 h and then at 120 °C for at least 18 h with yield ranging from 85

to 90 mol %. The materials were stored in sealed glass tubes in a controlled environment (dry-room, RH < 0.1% at 20 °C).

The water content in the ionic liquids was measured using the standard Karl Fisher method. The titrations were performed by an automatic Karl Fisher coulometer titrator (Mettler Toledo DL32) in a dry-room (RH < 0.1%) at 20 °C. The Karl Fisher titrant was a one-component reagent purchased from Aldrich (Hydranal 34836 Coulomat AG). Immediately after drying, the water content was below 2 ppm.

**Viscosity Measurements.** The viscosity measurements were carried out using a rheometer (HAAKE RheoStress 600) located in the dry-room. The tests were performed from 20 to 80 °C (1 °C/min heating rate) in the 100–2000 s<sup>−1</sup> rotation speed range. Viscosity values were taken at 10 °C step.

**Conductivity and Density Measurements.** The ionic conductivity of the PYR<sub>14</sub>TFSI, PYR<sub>14</sub>BETI, and PYR<sub>14</sub>IM<sub>14</sub> ionic liquid samples was determined by an AMEL 160 conductivity meter. The RTILs were housed in sealed, glass conductivity cells (AMEL 192/K1) equipped with two porous platinum electrodes (cell constant of 1.00 ± 0.01 cm). The cells were assembled in the dry-room (RH < 0.1% at 20 °C). The conductivity tests were performed in the temperature range from −40 to 100 °C by using a climatic test chamber (Binder GmbH MK53). The entire setup was controlled by software developed at ENEA. In order to fully crystallize the materials, the cells were immersed in liquid nitrogen for a few seconds and then transferred in the climatic chamber at −40 °C. After a few minutes of storage at this temperature, the solid but amorphous samples relaxed and turned again liquid. This route was repeated until the ionic liquids remained solid at −40 °C. In previous work, it was demonstrated that a not careful crystallization process of the ionic liquid may generate nonequilibrium states of the sample that affect the thermal properties as well as the conductivity results.<sup>28</sup> The PYR<sub>14</sub>IM<sub>14</sub> sample did not turn liquid even after repeated crystallization processes, suggesting a phase transition directly from an amorphous solid state to a liquid. Finally, after a storage period at −40 °C for at least 15 h the conductivity of the materials was measured in the −40 to 100 °C temperature range by running a heating scan at 2 °C/h.

For the purpose of comparison with the ion diffusion coefficients (see below), the RTIL conductivities ( $\sigma$ ) were converted into molar conductivities ( $\Lambda$ ), divided by the molar concentrations of the liquids:  $\Lambda = \sigma/c$ . In turn, the molar concentrations  $c$  are related to the density  $d$  through  $c = d/M$ , where  $M$  is the RTIL molar mass. The density measurements were performed from 80 to 20 °C by 10 °C step using a density meter (Mettler Toledo DE40) in a dry-room. The samples were previously degassed under a vacuum at 70 °C overnight to avoid bubble formation during the cooling scan tests.

**NMR Measurements.** The <sup>1</sup>H and <sup>19</sup>F NMR spectra were recorded on a Bruker Avance 500 spectrometer operating at 500 MHz proton frequency equipped with a QNP four nuclei switchable probe. Except where indicated, the NMR experiment was carried out at 305.0 ± 0.1 K. The preparation of the water-free samples for NMR measurements was done in a dry-room (vide supra). Suitable amounts (0.5–1.0 g each) of dry **1**, **2**, and **3** (water content below 2 ppm) were transferred in 5 mm NMR tubes previously heated under a vacuum and equipped with a sealed capillary containing d<sub>6</sub>-DMSO as the internal chemical shift reference and lock. The NMR tubes were flame-sealed immediately after the transfer of ionic liquids.

The {<sup>1</sup>H–<sup>1</sup>H}NOESY experiments were acquired with a mixing time ranging from 20 to 50 ms in steps of 5 ms for **2** and **3**, while longer mixing times (60–160 ms in steps of 20

ms) were needed for **1**. A total of 512 experiments were performed in the F1 dimension with 16 scans for each of the t1 increments and a sweep width of 3.9 ppm.  $\{^{19}\text{F}-^{19}\text{F}\}$  NOESY spectra were recorded with a sweep width of 80.5 ppm and 16 scans for each of the 512 increments. The mixing time ranged from 20 to 60 ms in steps of 10 ms. Heteronuclear  $\{^1\text{H}-^{19}\text{F}\}$  HOESY experiments were acquired using the inverse-detected pulse sequence<sup>29</sup> with 512 increments in the t1 dimension with 16 scans for each experiment. Qualitative spectra were acquired with a mixing time of 20, 30, and 40 ms.

Self-diffusion coefficients were measured by diffusion ordered correlation spectroscopy (DOSY) experiments by applying sine shaped pulsed magnetic field gradients along the *z*-direction up to a maximum strength of  $G = 53.5 \text{ G cm}^{-1}$ . All of the experiments were performed using the bipolar pulse longitudinal eddy current delay (BPLED) pulse sequence. Cation and anion self-diffusion coefficients were measured independently by carrying out DOSY experiments in the  $^1\text{H}$  and  $^{19}\text{F}$  frequency domains, respectively. The duration of the magnetic field pulse gradients ( $\delta$ ) and the diffusion delay ( $\Delta$ ) was optimized for each sample in order to obtain complete dephasing of the signals with the maximum gradient strength. In each DOSY experiment, a series of 16 spectra with 32K points were collected. For the investigated samples,  $\delta$  values were in the 8–12 and 15–20 ms ranges for  $^1\text{H}$  and  $^{19}\text{F}$  experiments, respectively, while the  $\Delta$  values were in the 0.12–0.5 and 0.10–0.5 s ranges for  $^1\text{H}$  and  $^{19}\text{F}$  experiments, respectively. The pulse gradients were incremented from 2 to 95% of the maximum gradient strength in a linear ramp. Variable temperature experiments were performed on samples **1** and **3** in the temperature range 300–340 K. The temperature was set to 305 K for sample **2**, and for all samples, the acquisition was controlled with an air flow of  $535 \text{ L h}^{-1}$  in order to avoid any temperature fluctuations due to sample heating during the magnetic field pulse gradients.

The measurement of the diffusion coefficients  $D$  was achieved by fitting the observed echo intensity  $I$  by the Stejskal–Tanner equation:

$$I = I_0 \exp\left[-(\gamma g \delta)^2 D \left(\Delta - \frac{\delta}{3}\right)\right] \quad (1)$$

where  $I_0$  is the echo intensity without field gradient,  $\gamma$  is the gyromagnetic ratio of the observed nucleus, and  $g$  is the maximum magnetic field gradient strength. The  $D$  diffusion coefficient is extracted from the slope of a linear fit of  $\ln(I/I_0)$  versus  $g^2$ . It is important to note that eq 1 was derived for rectangular gradient pulses and can be used for sine shaped gradient pulses provided the maximum gradient strength  $G$  values are multiplied by the factor  $2/\pi$  (i.e.,  $g = G \times (\text{ramp attenuation factor}) \times (2/\pi)$ ).<sup>30</sup> The procedure has been tested on a sample of deuterated methanol obtaining the literature value ( $2.11 \times 10^{-9} \text{ m}^2 \text{ s}^{-1}$  at  $25^\circ\text{C}$ ).

**Computational Procedures.** Computational studies were carried out for the  $\text{PYR}_{14}\text{TFSI}$  ion pair, in the gas phase. All calculations were performed with the Gaussian 03 program.<sup>31</sup> Stable structures were obtained in three sequential steps: (i) optimization of the ion geometries at the semiempirical level (PM3);<sup>32</sup> (ii) refinement of the minimum-energy structures for the isolated ions by ab initio density functional theory (DFT) calculations (B3LYP hybrid functional with the 6-311G(d) basis set<sup>33</sup>); (iii) docking of the cation and anion with different starting orientations (overall, 20 different geometries), followed by energy minimizations of the pair at the same DFT level. A vibrational analysis was performed at the same level on the final

geometries, where a lack of imaginary frequencies confirms that they represent minimum-energy structures. We point out that common DFT methods (including B3LYP) do not account properly for the dispersion interaction,<sup>34</sup> but presumably this is only a small fraction of an interaction dominated by electrostatics. Similarly, an estimate of the basis set superposition error (BSSE) by application of the counterpoise<sup>34</sup> method to the minimum-energy ion pair shows that this is of the order of 15 kJ/mol, which represents only 5% of the total interaction energy (about 300 kJ/mol). Hence, all of the results to be presented below were obtained without any BSSE correction.

### 3. Results and Discussion

**Intermolecular Contacts via Nuclear Overhauser Enhancements.** The molecular formulas and atom numbering of  $\text{PYR}_{14}\text{TFSI}$  (**1**),  $\text{PYR}_{14}\text{BETI}$  (**2**), and  $\text{PYR}_{14}\text{IM}_{14}$  (**3**) are reported in Scheme 1. The reference  $^1\text{H}$  and  $^{19}\text{F}$  NMR spectra of the pure liquids are displayed in Figure 1 along with the spectral assignment. For both nuclei, high-resolution spectra can be obtained despite the high viscosity of the samples. Ring protons in equivalent positions are isochronous; thus, pseudoaxial and pseudoequatorial hydrogen atoms cannot be distinguished.

As previously reported, useful information for the assessment of the local structure of the titled pure liquids can be obtained by 2D NMR correlation spectroscopy based on the nuclear Overhauser enhancement (NOE). This approach was successfully applied to the investigation of the local structure of model RTILs and to derive a picture of short-range aggregation motives in imidazolium-based RTILs.<sup>35–41</sup> More recently, it has been applied to the investigation of proton transfer and aggregation phenomena in proton conducting ILs.<sup>42</sup> The method is based on the mutual spin–spin relaxation of nuclei close in space and mediated by dipolar interactions (cross-relaxation). According to the theory,<sup>43</sup> in the case of intramolecular cross-relaxation (e.g., NOE provided by nuclei close in space and belonging to the same molecule), the cross-relaxation is dominated by rotational tumbling of the molecule, leading to the  $r^{-6}$  distance dependency of the NOE intensity ( $r$  being the internuclear distance of the cross-relaxing nuclei). Therefore, only short-range and specific interactions are expected to give rise to NOE and the threshold  $r = 4 \text{ \AA}$  is commonly accepted for vanishing NOEs. Conversely, if the cross-relaxing nuclei belong to different molecules in the chemical exchange regime (e.g., solute–solvent interaction, solvation of proteins, etc.), then the cross-relaxation is dominated by translational diffusion, leading to  $r^{-1}$  distance dependency of the NOE intensity.<sup>44,45</sup> A dramatic consequence is that long-range, nonspecific NOEs are also expected, thus limiting the structural use of NOE data with the current interpretative tools. Here, we adopt the reasonable assumption that, for highly associated systems such as long-lived clusters or locally structured liquids, intermolecular NOEs can be interpreted as intramolecular ones.<sup>46,47</sup> Nevertheless, cautious use of intermolecular NOE data for the assessment of aggregation geometries or specific intermolecular interactions is advisable. Therefore, we will discuss the intermolecular NOE data in a semiquantitative way, without attempting to derive quantitative estimates of the intermolecular distances within the liquid.

Despite the fact that homonuclear  $\{^1\text{H}-^1\text{H}\}$  and  $\{^{19}\text{F}-^{19}\text{F}\}$  NOE data can potentially provide details of cation–cation and anion–anion organization also in the case of pyrrolidinium-based ILs with fluorine containing anions, our results were not as clear-cut as in the other cases mentioned above.<sup>39</sup> Signal overlap and difficulties in distinguishing genuine intermolecular NOEs from intramolecular ones hampered the interpretation of homonuclear experiments carried out on **1**, **2**, and **3**. Conversely, heteronuclear  $\{^1\text{H}-^{19}\text{F}\}$

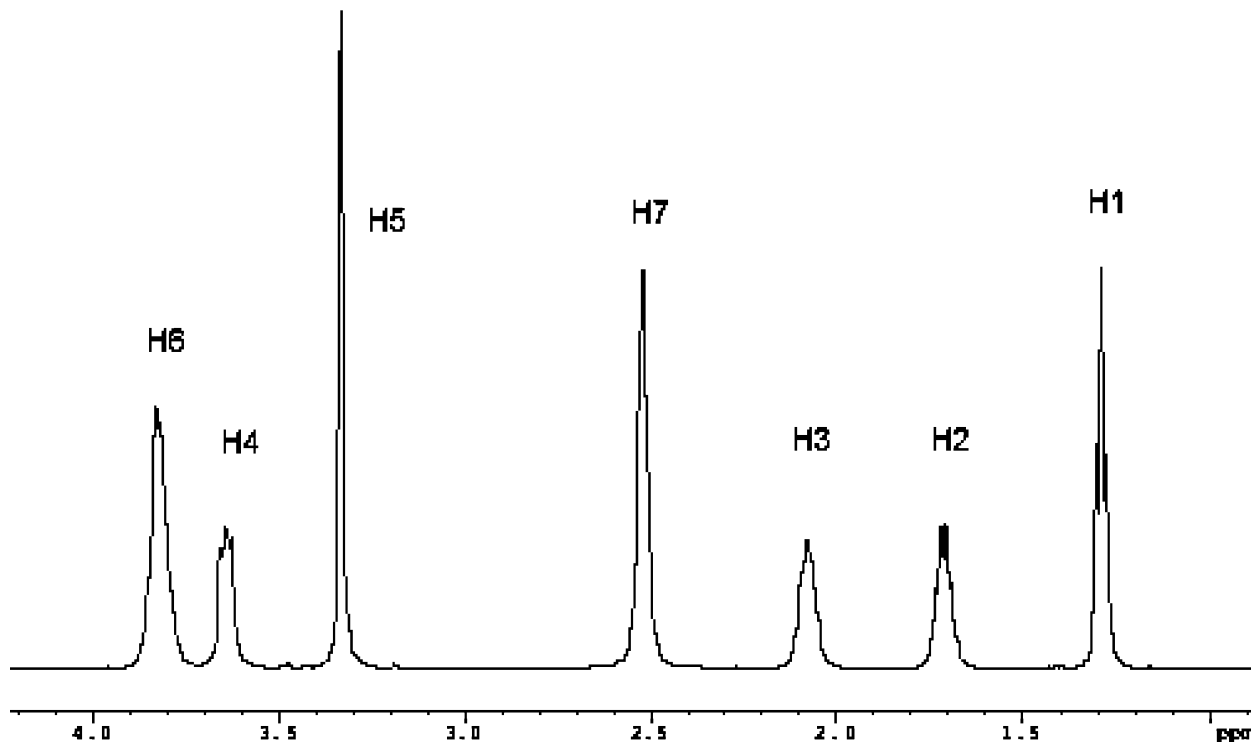


Figure 1.  $^1\text{H}$ -NMR spectrum of pure material **1**. Atom numbering is reported in Scheme 1.

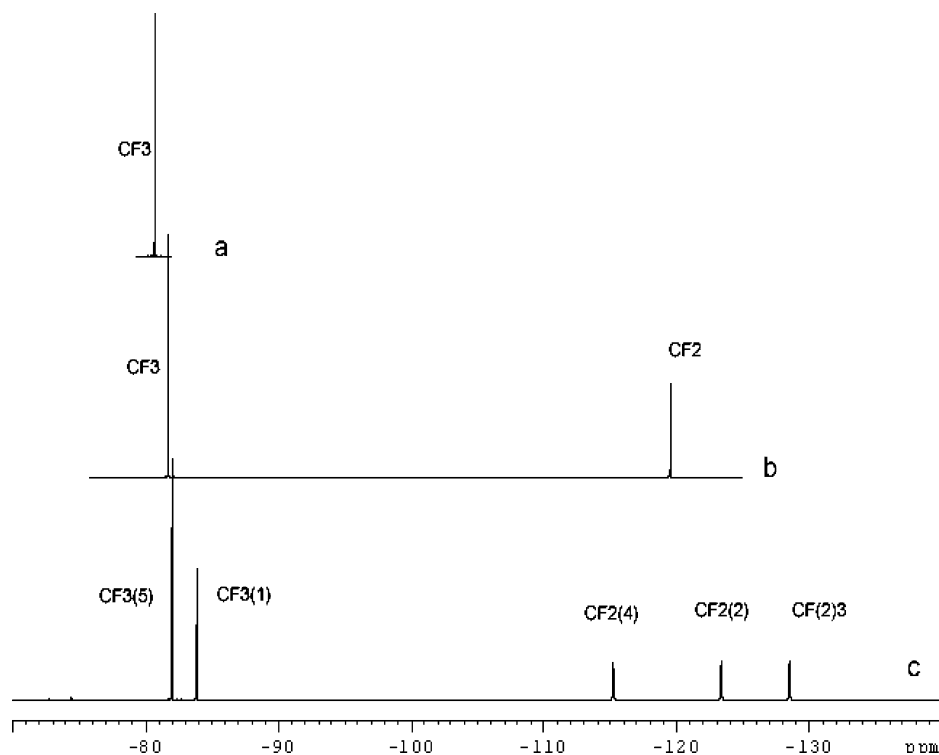


Figure 2.  $^{19}\text{F}$ -NMR spectra of materials **1** (trace a), **2** (trace b), and **3** (trace c). The numbers on the peaks refer to the atom numbering of the corresponding structure.

NOE correlation experiments (HOESY) on titled compounds showed dipolar contacts between selected protons of the cation and selected F nuclei of the anions, providing valuable information on cation–anion interactions and aggregation motives. Therefore, the discussion on the local structure of **1**, **2**, and **3** is mainly based on HOESY data. Cross-peak intensities are reported in Table 1. The first column contains the atom type and numbering of the cation (see Scheme 1). NOE data related to the interactions of  $\text{PYR}_{14}$  with  $\text{CF}_3$  of **1** are reported in the second column. Data

related to the  $\text{CF}_2$  and  $\text{CF}_3$  of **2** are reported in columns 2 and 3, respectively, while the remaining columns contain the NOE data of the five groups of nonequivalent F atoms present in the anion of compound **3**.

Figure 3 shows the contour plot of the HOESY experiment on pure **1**. The most striking feature is the selective pattern of observed NOEs. Indeed, the  $\text{CF}_3$  group of the anion shows selective contacts with H6, H7, and H5, namely, the protons belonging to the pyrrolidinium ring and the *N*-methyl group of the cation. On the



**TABLE 1: Relative  $\{^1\text{H}-^{19}\text{F}\}$  NOE Intensity for Cross-Peak Integration of HOESY<sup>a</sup> Spectra of Materials 1, 2, and 3**

	Pyr <sub>14</sub> TFSI (1)		Pyr <sub>14</sub> BETI (2)		Pyr <sub>14</sub> IM <sub>14</sub> (3)			
	CF <sub>3</sub>	CF <sub>2</sub>	CF <sub>3</sub>	CF <sub>3</sub> (1)	CF <sub>2</sub> (2)	CF <sub>2</sub> (3)	CF <sub>2</sub> (4)	CF <sub>3</sub> (5)
CH <sub>3</sub> (1)	0.62	0.07	0.29	0.30	0.10	0.07	0.10	0.4
CH <sub>2</sub> (2)								0.05
CH <sub>2</sub> (3)								0.11
CH <sub>2</sub> (4)								0.11
CH <sub>2</sub> (6)	0.63	0.13	0.38	0.11	0.124	0.19	0.25	0.87
CH <sub>2</sub> (7)	0.37	0.40	0.88	0.36	0.19	0.25	0.13	0.94
CH <sub>3</sub> (5)	1	0.64	1	0.29	0.23	0.33	0.33	1

<sup>a</sup>Experiments were carried out with a 40 ms mixing time. The cross-peak volume relating CH<sub>3</sub>(5) of the cation with NSOCF<sub>3</sub> of the anion was arbitrarily set to 1 in all cases. All of the volumes were normalized by the factor  $(n_{\text{H}}n_{\text{F}}/n_{\text{H}} + n_{\text{F}})$ , where  $n_{\text{H}}$  and  $n_{\text{F}}$  are the number of equivalent proton and fluorine nuclei giving rise to NOE, respectively.

contrary, the NOE intensities related to interaction of the CF<sub>3</sub> with the *n*-butyl chain of the cation, namely, H2, H3, and H4, are below the noise level. These findings suggest that anions belonging to the coordination shell of a given cation adopt specific and nonrandom orientations. Interestingly, the single crystal structure of **1** reported in the literature<sup>48</sup> clearly shows a pattern of short intermolecular contacts (<3.5 Å) fully consistent with those derived from NOEs in the bulk liquid and described above, thus confirming the resemblance of the structure found in the crystalline state of some ILs with the nanostructure deduced from spectroscopic studies on the liquid. The apparently anomalous  $\{^1\text{H}-^{19}\text{F}\}$  NOE signal between the CF<sub>3</sub> groups and the terminal CH<sub>3</sub>(1) protons of the butyl could be explained by admitting the existence of long-range dipolar interactions exceeding the first coordination layer, as mentioned above.

The previous conclusions are supported by the data of further HOESY experiments on samples **2** and **3**. The corresponding contour plots are reported in Figures 4 and 5, respectively. In compound **2**, both CF<sub>2</sub> and CF<sub>3</sub> groups of the short perfluoroethyl chains provide the same NOE pattern discussed above for the reference TFSI anion, supporting the conclusion that the fluorine moieties do not show any tendency to interact with the linear hydrocarbon chain of the cation. This conclusion is further validated by the results of HOESY experiments on **3**. The sulfonylimido group of IM<sub>14</sub> anion is nonsymmetrically substituted with an isolated CF<sub>3</sub> group on one side and a perfluorinated C<sub>4</sub> linear chain on the other. The NMR signals belonging to the CF<sub>3</sub> groups are not overlapped and can be distinguished. The contour plot of the HOESY experiment (Figure 5) and quantitative data of Table 1 point out that all CF<sub>2</sub> groups of the perfluorobutyl chain are selectively close in space to H5, H6, and H7, namely, to the pyrrolidinium ring and to the *N*-methyl group. The CF<sub>3</sub> group in position 1 (see Scheme 1) shows the same pattern of intermolecular NOEs. It is interesting to note that the isolated CF<sub>3</sub> group in position 5 provides a far less selective NOE pattern. Indeed, as reported in Table 1, the isolated CF<sub>3</sub> gives strong interactions with H6, H7, and H5 of the cation (relative intensities of 0.87, 0.94, and 1, respectively) and weak interactions with CH<sub>2</sub> groups in positions 2, 3, and 4 (relative intensities of 0.05, 0.11, and 0.11, respectively).

The general conclusion consistent with these intermolecular NOE results is that two main driving forces contribute to the local RTIL structure: Coulomb attractions, combined with the slow dynamics of these liquids, account for the existence of long-lived associations,<sup>49</sup> while the general tendency to avoid unfavorable hydrocarbon–perfluorocarbon contacts<sup>50</sup> is expected to provide preferential orientation of the anion and cation within the aggregates. This interpretation is consistent with the observed

high selectivity with respect to the Pyr<sub>14</sub> cation of CF<sub>3</sub>(1), located at the end of the perfluorobutyl chain of IM<sub>14</sub>, and the lower selectivity shown by the isolated CF<sub>3</sub>(5) of the same anion. As a possible consequence of these findings, the segregation of hydrocarbon and perfluorocarbon moieties at the molecular level with the formation of fluorine mesoscopic domains can be hypothesized in this case. This is indeed confirmed by the crystals of **1**,<sup>48</sup> which display a layered structure with an alternation of cations and anions.

**Viscosity, Conductivity, and Diffusion Coefficients.** In many of the practical applications mentioned in the Introduction, the main interest lies in “dynamic” rather than “structural” properties of the RTILs. Examples are the viscosity, ion diffusion, and conductivity. Because of their high viscosity and scarce propensity to crystallization, the dynamic behavior of RTILs resembles that of other supercooled liquids<sup>51,52</sup> and, typically, they can be classified as “fragile” glass formers.<sup>53</sup>

At 30 °C, **1**, **2**, and **3** find fairly high shear viscosities, respectively, of 60, 200, and 290 mPa·s (the value for **1** is in perfect agreement with that previously reported by Tukuda et al.<sup>54</sup>). Figure 6 contains plots showing the temperature dependence of their viscosity  $\eta$ , or equivalently their fluidity  $\phi = \eta^{-1}$ . Over the investigated temperature range, they can be fitted reasonably well by the Arrhenius function,  $\phi(T) = \phi_{\infty} \exp(-E_a/RT)$  (the related Vogel–Fulcher–Tamman function<sup>51–53</sup> would provide an even better fit, but it contains one more adjustable parameter). The activation energies  $E_a$  increase with increasing anion size and complexity, from 29 kJ/mol for Pyr<sub>14</sub>TFSI, to 37 kJ/mol for Pyr<sub>14</sub>BETI, to 41 kJ/mol for Pyr<sub>14</sub>IM<sub>14</sub>.

The self-diffusion coefficients of anion and cation for **1**, **2**, and **3** were measured independently by DOSY experiments in the  $^{19}\text{F}$  and  $^1\text{H}$  frequency domains, respectively. The details are reported in the experimental section. Figure 7 shows the linear regression yielding the  $D$  values for cation and anion of material **2**. The resulting self-diffusion coefficients at 32 °C for all of the examined liquids are reported in Table 2. Again, the values for **1** are in good agreement with those reported by Tukuda et al.<sup>54</sup>

It is interesting to compare the  $D$  values for the anion and cation within the same liquid. For all of the examined compounds, the values of self-diffusion coefficients of cation and anion are close but significantly different, even considering the associated uncertainties. In all cases, we find  $D_{\text{cation}} > D_{\text{anion}}$ , indicating a somewhat larger mobility of cations compared to the negative counterpart. In the context of solution chemistry, the observation of identical values for the diffusion coefficients of the cation and the anion is interpreted as a diagnostic of complete ion pairing, while small deviations from unity of the  $D_+/D_-$  ratio are interpreted as intermediate ion pairing.<sup>55</sup> However, the concept of “ion pair” in bulk RTILs is not unanimously accepted and still open to debate. It is invoked in authoritative papers,<sup>56</sup> but this probably represents an oversimplification. Rather, ion clustering, as postulated by Earle et al. for explaining the volatility of RTILs,<sup>57</sup> or even larger aggregations, as depicted by Xiao et al. on the basis of Raman-induced Kerr effect spectroscopy studies,<sup>58</sup> seem to propose a more realistic picture able to rationalize the observed behaviors of RTILs.

The large increase in  $D$  on passing from **3** to **1**—in particular for the Pyr<sub>14</sub><sup>+</sup> cation, which is common to all of these liquids—can be related to their marked differences in viscosity. At the simplest possible level, we have the Stokes–Einstein relationship, which assimilates the ions to solid spheres of radius  $R$  moving in a homogeneous viscous medium and predicts that

$$D \propto \frac{k_{\text{B}}T}{\eta R} \quad (3)$$

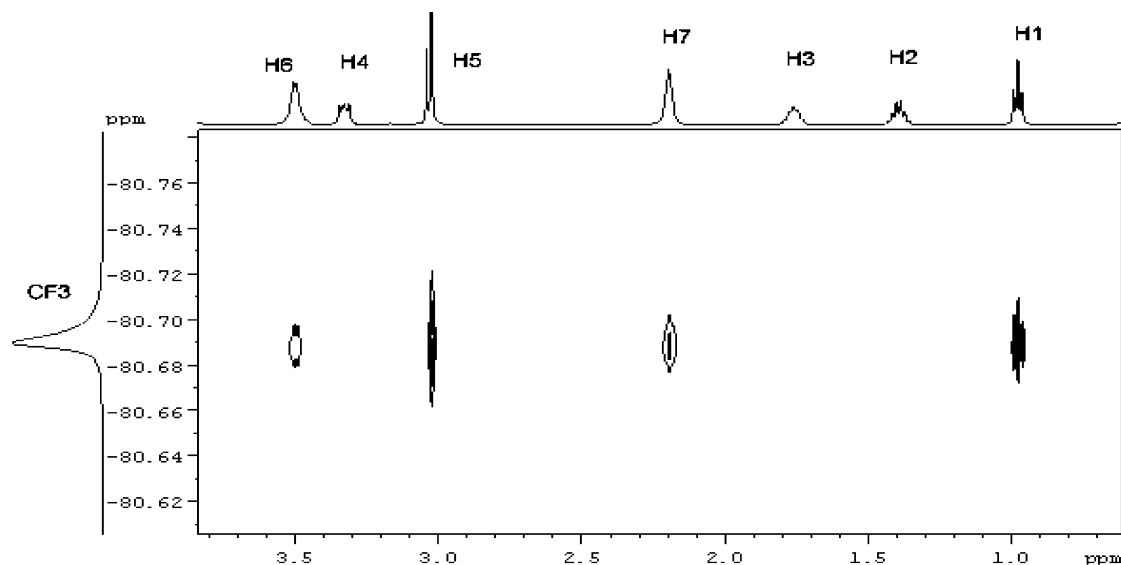


Figure 3. Contour plot of the HOESY experiment on material 1. Atom numbering according to Scheme 1.

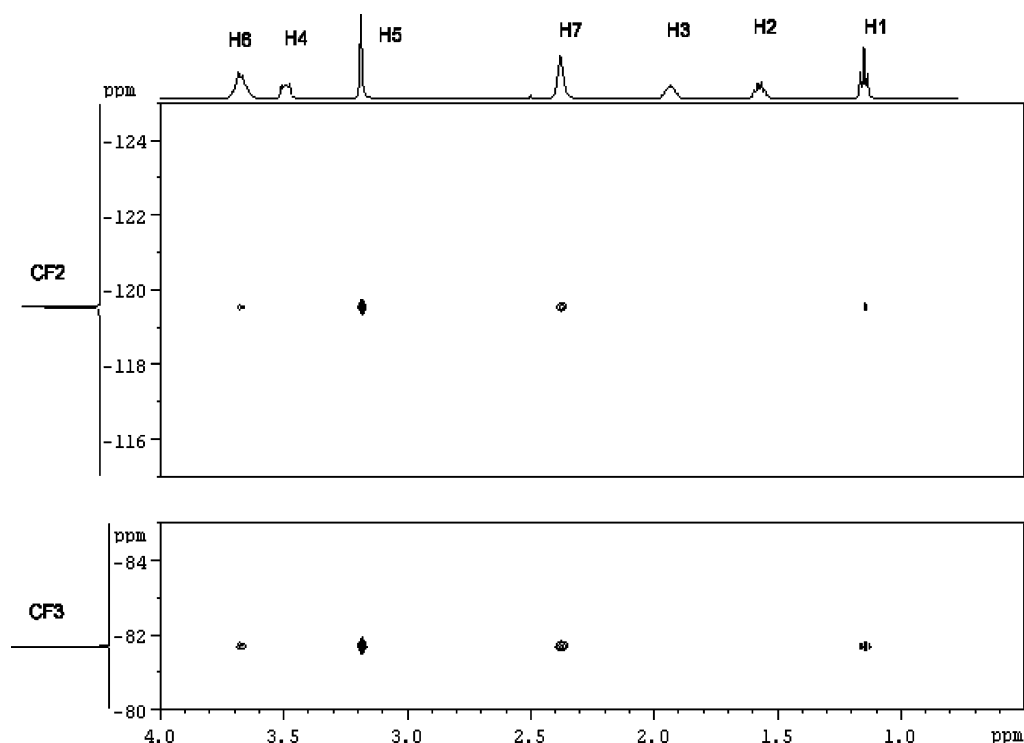


Figure 4. Contour plot of the HOESY experiment on material 2. Atom numbering according to Scheme 1.

This does not hold in the present case, as can be checked by computing the product  $D(\text{PYR}_{14}^+) \times \eta$ , which takes different values for each of the three ILs. This breakdown of the Stokes–Einstein relationship could be explained by admitting that the cation has an anion-dependent effective radius or, perhaps more convincingly, by remembering that the motions of cations and anions must be strongly coordinated. Even so, there is a clear correlation between viscosity and diffusion, which is demonstrated by the temperature dependence of the ion diffusion coefficients in **3**. The results are shown in Figure 8, in the Arrhenius representation. It is remarkable that the cation and the anion of  $\text{PYR}_{14}\text{IM}_{14}$  have practically the same temperature dependency, characterized by an activation energy of 43 kJ/mol, which is very close to the activation energy for its viscosity. Similarly, if we use the data for  $\text{PYR}_{14}\text{TFSI}$  reported by Tokuda et al.,<sup>54</sup> we find that the activation energies for the

cation and anion diffusion are both equal to 34 kJ/mol. This confirms that the closeness of the two ion diffusion coefficients is not accidental, but it reflects a more fundamental property in the dynamics of these liquids.

Table 2 also reports the experimental values of conductivities of **1**, **2**, and **3**. The molar conductivities ( $\Lambda$ ) are compared to the values calculated by the Nernst–Einstein equation ( $\Lambda_{\text{NE}}$ ) through the  $D_+$  and  $D_-$  diffusion coefficients according to eq 4:

$$\Lambda_{\text{NE}} = \frac{N_A e^2}{k_B T} (z_+^2 D_+ + z_-^2 D_-) \quad (4)$$

where  $N_A$  is the Avogadro number,  $e$  is the elementary charge,  $z_i$  is the valence of ion  $i$  ( $\pm 1$  in this case),  $k_B$  is the Boltzmann

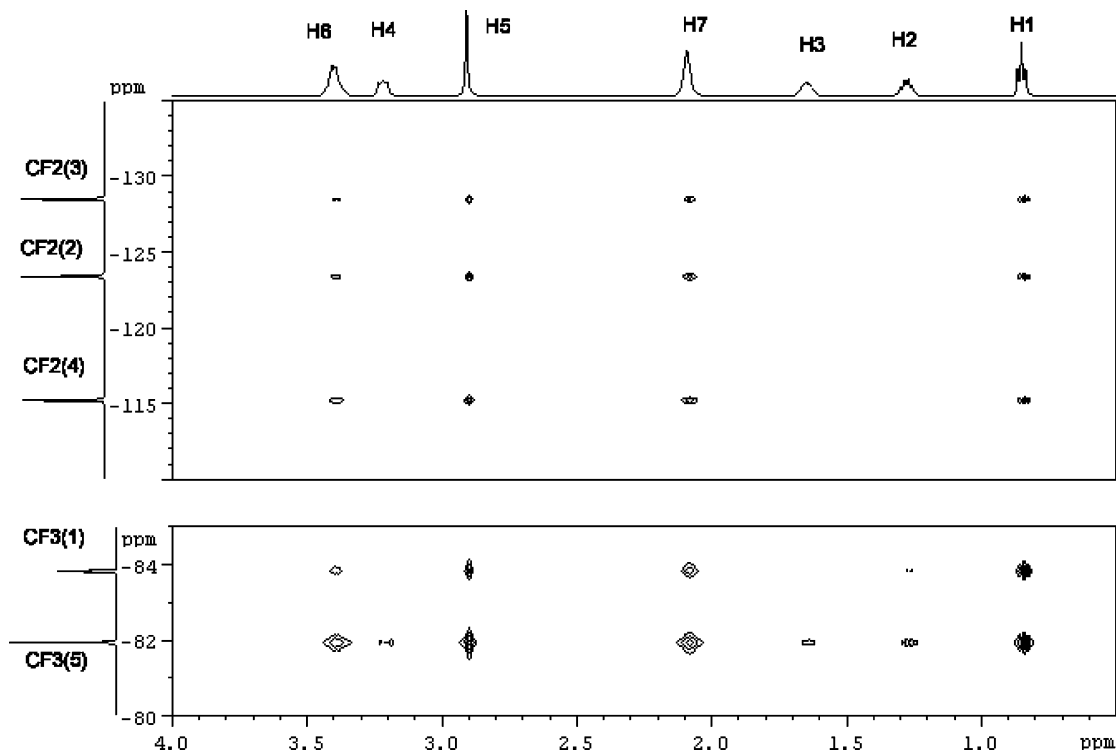


Figure 5. Contour plot of the HOESY experiment on material 3. Atom numbering according to Scheme 1.

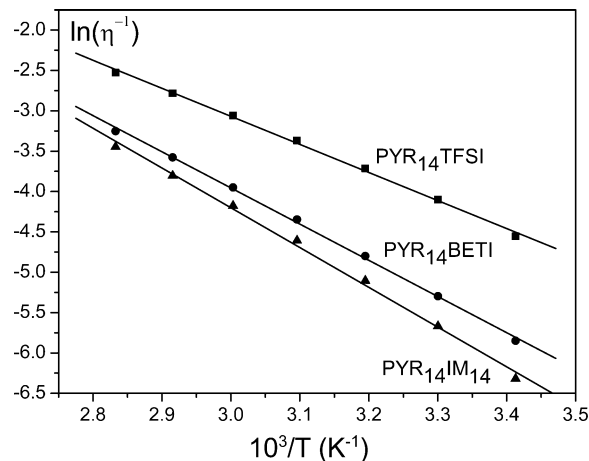


Figure 6. Arrhenius plots, showing the temperature dependence of the fluidity (reciprocal of the viscosity) for materials 1, 2, and 3.

constant, and  $T$  is the absolute temperature. Equation 4 is actually an approximation to a more general expression, relating the conductivity to the individual ionic motions:<sup>23</sup>

$$\Lambda_{\text{FULL}} = \frac{N_A e^2}{k_B T} \lim_{t \rightarrow \infty} \sum_{ij} z_i z_j \frac{\langle \Delta \mathbf{R}_i(t) \cdot \Delta \mathbf{R}_j(t) \rangle}{6t} \quad (5)$$

where  $\langle \dots \rangle$  denotes an ensemble average and  $\Delta \mathbf{R}_i(t)$  is the displacement of ion  $i$  over time  $t$ . Equation 4 is recovered by neglecting all correlations in the ionic displacements and retaining only the diagonal terms ( $i = j$ ), and remembering that the diffusion coefficients of an ion is  $D_i = \lim_{t \rightarrow \infty} \langle \Delta \mathbf{R}_i^2(t) \rangle / 6t$ . Clearly, the assumption of independent ion motions is justified only for dilute solutions but will break down at finite concentrations either because of ion pair formation<sup>49</sup> or—as in the present case of bulk ionic liquids—because of complex many-body correlations. Such cor-

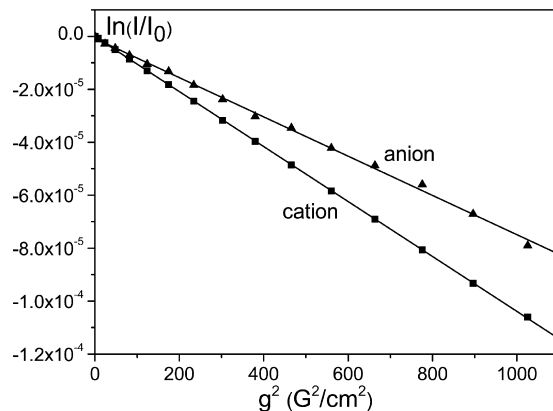


Figure 7. DOSY data at 305 K for material 2.

relations are not specific to RTILs, but they are well-known to exist also in conventional molten salts. For example, the mean value of the ratio  $R = \Lambda / \Lambda_{\text{NE}}$  is equal to 0.74 in molten alkali halides.<sup>59</sup>

The data of Table 2 indicate a strong decrease in conductivity on going from 1 to 2, and a much smaller one on going from 2 to 3. This qualitative feature is captured also by the simplified Nernst–Einstein relationship. On the other hand, we find rather small values of  $R$ , implying strong quantitative deviations from the Nernst–Einstein predictions. As explained above, at a fundamental level, these must be ultimately due to correlations in the ion motions. Unfortunately, at present, we cannot give a simple “pictorial” model for the precise nature of these correlations. A reasonable interpretation, consistent also with the other data, would be the formation of mesoscopic domains within the RTILs, connected to the aggregation of the butyl and perfluorobutyl chains. These domains could be either *structurally* heterogeneous or possibly, in analogy with recent findings in the field of supercooled liquids, *dynamically* heterogeneous.<sup>51,52,60</sup>

**DFT Calculations in Ion Pairs.** As discussed above, the notion of ion pairs in RTILs has been strongly challenged by

TABLE 2: Experimental Physical Properties of Materials 1, 2, and 3 at 305 K<sup>a</sup>

RTIL sample	$c$ , mol cm <sup>-3</sup>	$\eta$ , mPa·s	$\sigma$ , S·cm <sup>-1</sup>	$\Lambda$ , S·cm <sup>2</sup> ·mol <sup>-1</sup>	$D_{\text{cation}}$ , <sup>b</sup> cm <sup>2</sup> s <sup>-1</sup>	$D_{\text{anion}}$ , <sup>c</sup> cm <sup>2</sup> s <sup>-1</sup>	$\Lambda_{\text{NE}}$ , <sup>d</sup> S·cm <sup>2</sup> ·mol <sup>-1</sup>	$R$
PYR <sub>14</sub> TFSI (1)	$3.37 \times 10^{-3}$	60	$2.84 \times 10^{-3}$	0.843	$(25.11 \pm 0.15) \times 10^{-8}$	$(19.76 \pm 0.20) \times 10^{-8}$	1.647	0.512
PYR <sub>14</sub> BETI (2)	$2.87 \times 10^{-3}$	200	$0.774 \times 10^{-3}$	0.270	$(9.02 \pm 0.03) \times 10^{-8}$	$(6.24 \pm 0.06) \times 10^{-8}$	0.560	0.482
PYR <sub>14</sub> IM <sub>14</sub> (3)	$2.85 \times 10^{-3}$	290	$0.546 \times 10^{-3}$	0.192	$(6.44 \pm 0.02) \times 10^{-8}$	$(4.29 \pm 0.07) \times 10^{-8}$	0.394	0.486

<sup>a</sup> We report the molar concentrations  $c$ , the viscosities  $\eta$ , the conductivities  $\sigma$ , the molar conductivities  $\Lambda$ , and the NMR self-diffusion coefficients  $D$  of the cation and the anion. The last two columns contain the molar conductivities estimated from the NMR diffusion coefficients using the Nernst–Einstein relationship  $\Lambda_{\text{NE}}$  and the ratios  $R = \Lambda/\Lambda_{\text{NE}}$ . <sup>b</sup> From <sup>1</sup>H-DOSY. <sup>c</sup> From <sup>19</sup>F-DOSY. <sup>d</sup> See eq 4.

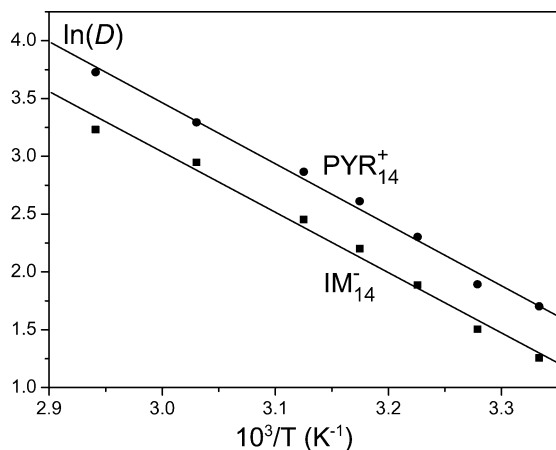


Figure 8. Arrhenius plots showing the temperature dependency of the ion diffusion coefficients in PYR<sub>14</sub>IM<sub>14</sub>.

some authors. On the other hand, ion pairs can certainly be regarded as the simplest “synthon” giving rise to more complex clustering. Thus, *ab initio* calculations on cation–anion pairs can provide first-principle information on the energetic and geometric features of the intermolecular interactions, which are vital for understanding the bulk liquids and for modeling larger aggregates.<sup>25</sup>

We have performed *ab initio* calculations of gas-phase ion pairs of **1**, as described in the methods section. The five-membered rings (C<sub>4</sub>N) of pyrrolidine and its *N*-methylated pyrrolidinium derivatives are not planar, and it is possible to have conformers of envelope or twist type. Many calculations have been performed on this type of structure (see ref 26 and references therein). The envelope-type conformation with the N atom above the C<sub>4</sub> plane and the N–CH<sub>3</sub> bond at the equatorial position has been identified as the most stable structure of *N*-methylpyrrolidine. The global minimum of the PYR<sub>14</sub><sup>+</sup> cation has an envelope conformation for the ring, with the butyl in the equatorial position and the methyl in the axial position. We repeated some of these calculations on the cation,<sup>26</sup> and in addition, we fully explored the conformational space of the butyl side chain by changing the  $\alpha$ ,  $\beta$ , and  $\gamma$  torsions in steps of 60°, keeping the equatorial-envelope structure of the *N*-methyl-C<sub>4</sub> ring. We found several local energy minima. The global one has an extended all-trans conformation of the butyl, confirming the results of ref 26. On the other hand, we found that the TFSI<sup>−</sup> anion has a single well-defined minimum, with the trifluoromethyl groups on opposite sides of the plane defined by the S–N–S atoms.

The relative arrangements of the anion and the cation were systematically investigated by optimizing the geometries of several PYR<sub>14</sub>TFSI pairs. Our starting structures comprised situations with the TFSI<sup>−</sup> anion above or below the pyrrolidinium ring, or at various positions along the butyl chain. Accordingly, the CF<sub>3</sub> groups of the anion interacted either with

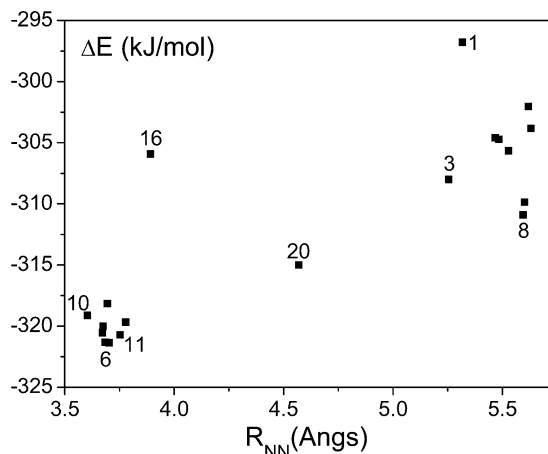


Figure 9. Stabilization energies of 20 different ion pair configurations for PYR<sub>14</sub>TFSI, calculated with respect to the minimum-energy structures of the isolated ions. The energies are plotted against the N–N distance. The numbers indicate the ion pairs which have been selected for representation in Figure 10.

the alkyl chain or the ring. In all cases, the starting point for each ion corresponded to its isolated minimum-energy structure.

At long range, the interaction among the ions can be roughly described in terms of Coulomb’s law for point charges, which are formally located on the two nitrogen atoms. On approaching their contact distance, this basic interaction will be modulated by other factors, connected with the complex shape, charge distribution, and polarizability of the ions. These factors are certainly important in differentiating RTILs from conventional ionic solids such as NaCl. The computational results are summarized in Figure 9, which presents a scatter plot of the ion pair energies against the N–N distance. Figure 10 shows the ion configurations within eight representative pairs. The scatter plot shows that, among all of the possible local minima, the ion pairs with the shortest N–N distance have the lowest energies. On the other hand, Coulomb interactions are not the only important structural principle. For example, the energy of ion pair 16 is about 5 kJ/mol higher than the one of 8, despite the fact that its centers of charge are 1.5 Å closer in space. All the low-energy structures, represented by the cluster of points at the lower left corner of Figure 9, are also characterized by the fact that the anion is positioned above (e.g., pairs 6 and 11) or to the side (pair 10) of the five-membered ring of the cation, minimizing the interference with the *N*-alkyl groups. This agrees with the observed heteronuclear NOE data.

It is also interesting to observe that the nearest-neighbor N–N distances which are found in the published crystal structure of PYR<sub>14</sub>TFSI fall in the range between 4.23 and 6.45 Å.<sup>48</sup> These are well above the N–N distances within the gas-phase structures with the lowest energies; see again Figure 9. This is not surprising, considering that in the solid state the ions must optimize the interactions with several other ions, all at the same time. Indeed, a related trend is seen also in the structure of



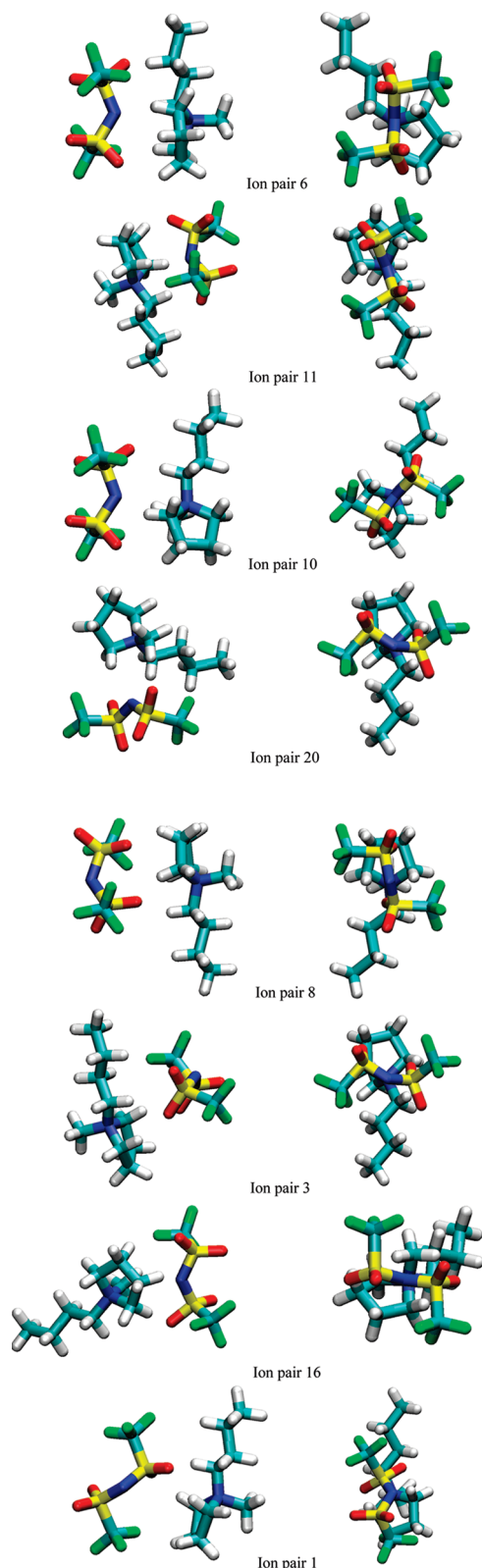


**Figure 10.** Selected ion pair configurations of **1** (two views for each structure). In the right-hand views, the nitrogen of  $\text{PYR}_{14}^+$  is always aligned behind the nitrogen of  $\text{TFSI}^-$ . The ion pairs are shown in order of increasing energy (see Figure 9).

conventional ionic solids, where there is a systematic increase in the ionic radii with increasing coordination number (c.n.).<sup>61</sup> For example, the tabulated radius of  $\text{Na}^+$  increases from 1.13 to 1.53 Å as the c.n. increases from 4 to 12. The radius of  $\text{O}^{2-}$  increases from 1.21 to 1.28 Å as the c.n. increases from 2 to 8.

It may be possible to perform a more detailed analysis and arrive at a clearer classification of the different ion pair configurations, either in terms of pairwise atomic interactions or by decomposition of the total interaction energy into its contributions (electrostatic, induction, dispersion, charge transfer, and Pauli repulsion, plus of course the intramolecular deformation energies).<sup>34</sup> We have not attempted to do this in this work. More simply, if a further lesson can be learned from the variety of structures displayed in Figure 10, it is that any relative motion of two oppositely charged ions within the bulk liquid cannot just consist of simple “sliding” movements but must involve rather complex intramolecular and intermolecular rearrangements. It is interesting to note that the energy spread between the lowest- and highest-energy structures in Figure 9 is about 25 kJ/mol, which is of the order of the activation energy measured from the temperature dependency of both the viscosity and the ion diffusion coefficients.

## Conclusions

Heteronuclear NOE techniques have been shown to be invaluable experimental tools for the assessment of the aggregation motives and structural organization of the titled compounds. The hypothesis of microsegregation of fluorine chains of the anions at molecular level (e.g., without observable phase separation) accounts for the observed selectivity of heteronuclear anion–cation NOE patterns with possible formation of fluorinated domains in materials **1**, **2**, and **3**. These conclusions could be conveniently exploited for optimizing the transport properties of  $\text{Li}^+$  ions in such media, in view of applications as components of new generation electrochemical devices.

The DOSY NMR method has been used to independently measure the self-diffusion coefficient of the cation ( $^1\text{H}$ ) and the anion ( $^{19}\text{F}$ ) in the ionic liquids. For all materials, we find  $D_{\text{cation}} > D_{\text{anion}}$ , indicating a higher degree of intermolecular organization of the anions, leading to lower mobilities. The temperature dependencies of the viscosities and ion diffusion coefficients in  $\text{PYR}_{14}\text{IM}_{14}$  and in  $\text{PYR}_{14}\text{TFSI}$  show similar Arrhenius-type behaviors, characterized by very close values of the activation energies for these processes. The marked difference between the experimental conductivities of these RTILs and those estimated from the NMR diffusion coefficients using the Nernst–Einstein relationship indicates a strong correlation in the ionic motions. This can be taken as further evidence for a nanoscale segregation in these systems, or possibly of dynamical heterogeneities such as those occurring in supercooled liquids approaching the glass transition temperature.<sup>60</sup>

*Ab initio* calculations on the  $\text{PYR}_{14}\text{TFSI}$  ion pairs agree with the observed heteronuclear NOE patterns, which show preferential interaction of the anion with the five-membered ring of the cation. Also, the calculated energy spread for the different ion pair configurations provides an interpretation of the activation energies of the liquids, as extracted from the temperature dependence of their viscosities and diffusion coefficients. Molecular dynamics simulations of the bulk ionic liquids are currently under way, with the aim to confirm and extend these preliminary interpretations.

**Acknowledgment.** S.P. and G.B.A. wish to thank European Commission within the FP6 STREP Projects ILHYPOS (Contract no. TST4-CT-2005-518307) and ILLIBATT (Contract no. NMP3-CT-2006-033181) for the financial support. The group of Politecnico di Milano acknowledges financial support from PRIN 2006 “*Materiali Organizzati Organico Funzionali*” and

from the Fondazione Cariplo. We thank two anonymous reviewers of the manuscript for stimulating criticism.

## References and Notes

- (1) Ishikawa, M.; Sugimoto, T.; Kikuta, M.; Ishiko, E.; Kono, M. *J. Power Sources* **2006**, *162*, 658–661.
- (2) Guerfi, A.; Duchesne, S.; Kobayashi, Y.; Vijh, A.; Zaghbi, K. *J. Power Sources* **2008**, *175*, 866–873.
- (3) Matsumoto, H.; Sakaebe, H.; Tatsumi, K.; Kikuta, M.; Ishiko, E.; Kono, M. *J. Power Sources* **2006**, *160*, 1308–1313.
- (4) Saint, J.; Best, A. S.; Hollenkamp, A. F.; Kerr, J.; Shin, J.-H.; Doeff, M. M. *J. Electrochem. Soc.* **2008**, *155*, A172–A180.
- (5) Shin, J.-H.; Henderson, W. A.; Scaccia, S.; Prosini, P. P.; Passerini, S. *J. Power Sources* **2006**, *156*, 560–566.
- (6) Shin, J.-H.; Henderson, W. A.; Tizzani, C.; Passerini, S.; Jeong, S.-S.; Kim, K.-W. *J. Electrochem. Soc.* **2006**, *153*, A1649–A1654.
- (7) Sakaebe, H.; Matsumoto, H.; Tatsumi, K. *Electrochim. Acta* **2007**, *53*, 1048–1054.
- (8) Nakagawa, H.; Fujino, Y.; Kozono, S.; Katayama, Y.; Nukuda, T.; Sakaebe, H.; Matsumoto, H.; Tatsumi, K. *J. Power Sources* **2007**, *174*, 1021–1026.
- (9) Shin, J.-H.; Henderson, W. A.; Passerini, S. *Electrochem. Solid-State Lett.* **2005**, *8*, A125–127.
- (10) Matsumoto, H.; Sakaebe, H.; Tatsumi, K. *J. Power Sources* **2005**, *146*, 45–50.
- (11) Sakaebe, H.; Matsumoto, H.; Tatsumi, K. *J. Power Sources* **2005**, *146*, 693–697.
- (12) Kobayashi, Y.; Mita, Y.; Seki, S.; Ohno, Y.; Miyashiro, H.; Terada, N. *J. Electrochem. Soc.* **2007**, *154*, A677–A688.
- (13) Yuyama, K.; Masuda, G.; Yoshida, H.; Sato, T. *J. Power Sources* **2006**, *162*, 1401–1408.
- (14) Balducci, A.; Henderson, W. A.; Mastragostino, M.; Passerini, S.; Simon, P.; Soavi, F. *Electrochim. Acta* **2005**, *50*, 2233–2237.
- (15) Lazzari, M.; Mastragostino, M.; Soavi, F. *Electrochem. Commun.* **2007**, *9*, 1567–1572.
- (16) Bennett, M. D.; Leo, D. J. *Sens. Actuators, B* **2004**, *115*, 79–90.
- (17) Ding, J.; Zhou, D.; Spinks, G.; Wallace, G.; Forsyth, S.; Forsyth, M.; MacFarlane, D. *Chem. Mater.* **2003**, *15*, 2392–2398.
- (18) Wang, J.; Xu, C.; Taya, M.; Kuga, Y. *Smart Mater. Struct.* **2007**, *16*, S214–219.
- (19) Yang, C.; Sun, Q.; Qiao, J.; Li, Y. *J. Phys. Chem. B* **2003**, *107*, 12981–12988.
- (20) Shao, Y.; Bazan, G. C.; Heeger, A. J. *Adv. Mater.* **2007**, *19*, 365.
- (21) Shin, J.-H.; Edman, L. J. *Am. Chem. Soc.* **2006**, *128*, 15568–15568.
- (22) Nicotera, I.; Oliviero, C.; Henderson, W. A.; Appetecchi, G. B.; Passerini, S. *J. Phys. Chem. B* **2005**, *109*, 22814–22819.
- (23) (a) Borodin, O.; Smith, G. D. *J. Phys. Chem. B* **2006**, *110*, 11481–11490. (b) Borodin, O.; Smith, G. D.; Henderson, W. *J. Phys. Chem. B* **2006**, *110*, 16879–16886.
- (24) (a) Weingartner, H. *Angew. Chem., Int. Ed.* **2008**, *47*, 654–670. (b) Chiappe, C. *Monatsh. Chem.* **2007**, *138*, 1035–1044.
- (25) (a) Tsuzuki, S.; Tokuda, H.; Hayamizu, K.; Watanabe, M. *J. Phys. Chem. B* **2005**, *109*, 16474–16481. (b) Hunt, P. A.; Kirchner, B.; Welton, T. *Chem.—Eur. J.* **2006**, *12*, 6762–6775. (c) Hunt, P. A.; Gould, I. R.; Kirchner, B. *Aust. J. Chem.* **2007**, *60*, 9–14. (d) Zahn, S.; Uhlig, F.; Thar, J.; Spickermann, C.; Kirchner, B. *Angew. Chem., Int. Ed.* **2008**, *47*, 3639–3641.
- (26) Fujimori, T.; Fuji, K.; Kanzaki, R.; Chiba, K.; Yamamoto, H.; Umebayashi, Y.; Ishiguro, S. *J. Mol. Liq.* **2007**, *131–132*, 216–224.
- (27) Appetecchi, G. B.; Scaccia, S.; Tizzani, C.; Alessandrini, F.; Passerini, S. *J. Electrochem. Soc.* **2006**, *153*, A1685–1691.
- (28) Henderson, W. A.; Passerini, S. *Chem. Mater.* **2004**, *16*, 2881–2885.
- (29) Alam, T. M.; Pedrotty, D. M.; Boyle, T. J. *Magn. Reson. Chem.* **2002**, *40*, 361–365.
- (30) Orosz, L.; Batta, Gy.; Kéki, S.; Nagy, N.; Deák, G.; Zsuga, M. *Carbohydr. Res.* **2007**, *342*, 1323–1328.
- (31) Frisch, M. J.; Trucks, G. W.; Schlegel, H. B.; Scuseria, G. E.; Robb, M. A.; Cheeseman, J. R.; Montgomery, J. A., Jr.; Vreven, T.; Kudin, K. N.; Burant, J. C.; Millam, J. M.; Iyengar, S. S.; Tomasi, J.; Barone, V.; Mennucci, B.; Cossi, M.; Scalmani, G.; Rega, N.; Petersson, G. A.; Nakatsuji, H.; Hada, M.; Ehara, M.; Toyota, K.; Fukuda, R.; Hasegawa, J.; Ishida, M.; Nakajima, T.; Honda, Y.; Kitao, O.; Nakai, H.; Klene, M.; Li, X.; Knox, J. E.; Hratchian, H. P.; Cross, J. B.; Bakken, V.; Adamo, C.; Jaramillo, J.; Gomperts, R.; Stratmann, R. E.; Yazyev, O.; Austin, A. J.; Cammi, R.; Pomelli, C.; Ochterski, J. W.; Ayala, P. Y.; Morokuma, K.;
- Voth, G. A.; Salvador, P.; Dannenberg, J. J.; Zakrzewski, V. G.; Dapprich, S.; Daniels, A. D.; Strain, M. C.; Farkas, O.; Malick, D. K.; Rabuck, A. D.; Raghavachari, K.; Foresman, J. B.; Ortiz, J. V.; Cui, Q.; Baboul, A. G.; Clifford, S.; Cioslowski, J.; Stefanov, B. B.; Liu, G.; Liashenko, A.; Piskorz, P.; Komaromi, I.; Martin, R. L.; Fox, D. J.; Keith, T.; Al-Laham, M. A.; Peng, C. Y.; Nanayakkara, A.; Challacombe, M.; Gill, P. M. W.; Johnson, B.; Chen, W.; Wong, M. W.; Gonzalez, C.; Pople, J. A. *Gaussian 03*, revision B.04; Gaussian, Inc.: Wallingford, CT, 2004.
- (32) (a) Stewart, J. J. P. *J. Comput. Chem.* **1989**, *10*, 209. (b) Stewart, J. J. P. *J. Comput. Chem.* **1989**, *10*, 221.
- (33) Koch, W.; Holthausen, M. C. *A Chemist's Guide to Density Functional Theory*; Wiley VCH: Weinheim, DE, 2000.
- (34) Stone, A. J. *The Theory of Intermolecular Forces*; Clarendon Press: Oxford, U.K., 1996.
- (35) Mantz, R. A.; Trulove, P. C.; Carlin, R. T.; Osteryoung, R. A. *Inorg. Chem.* **1995**, *34*, 3846–3847.
- (36) Dupont, P. J.; Suarez, A. Z.; De Souza, R. F.; Burrow, R. A.; Kintzinger, J.-P. *Chem.—Eur. J.* **2000**, *6*, 2377–2381.
- (37) Heimer, N. E.; Del Sesto, R. E.; Carper, W. R. *Magn. Reson. Chem.* **2004**, *42*, 71–75.
- (38) Mele, A.; Tran, C. D.; De Paoli Lacerda, S. H. *Angew. Chem., Int. Ed.* **2003**, *42*, 4364–4366.
- (39) Mele, A.; Romanò, G.; Giannone, M.; Ragg, E.; Fronza, G.; Raos, G.; Marcon, V. *Angew. Chem., Int. Ed.* **2006**, *45*, 1123–1126.
- (40) Mele, A. In *Ionic Liquids IIIA: Fundamentals. Progress. Challenges and Opportunities*; Rogers, R., Seddon, K. R., Eds.; ACS Symposium Series 901; American Chemical Society: Washington, DC, 2005; pp 2–17.
- (41) Nama, D.; Kumar, P. G. A.; Pregosin, P. S.; Geldbach, T. J.; Dyson, P. J. *Inorg. Chim. Acta* **2006**, *359*, 1907–1911.
- (42) Judeinstein, P.; Ioioiu, C.; Sanchez, J.-Y.; Ancian, B. *J. Phys. Chem. B* **2008**, *112*, 3680–3683.
- (43) Neuhaus, D.; Williamson, M. P. *The Nuclear Overhauser Effect in Structural and Conformational Analysis*; Wiley VCH: New York, 2000.
- (44) Halle, B. J. *Chem. Phys.* **2003**, *119*, 12372–12385.
- (45) Frezzato, D.; Rastrelli, F.; Bagno, A. *J. Phys. Chem. B* **2006**, *110*, 5676–5689.
- (46) Bagno, A.; Rastrelli, F.; Saielli, G. *Prog. Nucl. Magn. Reson. Spectrosc.* **2005**, *47*, 41–93.
- (47) Moreno, M.; Castiglione, F.; Mele, A.; Pasqui, C.; Raos, G. *J. Phys. Chem. B* **2008**, *112*, 7826–7836.
- (48) Choudhury, A. R.; Winterton, N.; Steiner, A.; Cooper, A. I.; Johnson, K. A. *J. Am. Chem. Soc.* **2005**, *127*, 16792–16793.
- (49) Marcus, Y.; Heft, G. *Chem. Rev.* **2006**, *106*, 4585–4621.
- (50) Smart, B. E. In *Organofluorine Chemistry: Principles and Commercial Applications*; Banks, R. E., Smart, B. E., Tatlow, J. C., Eds.; Plenum Press: New York, 1994.
- (51) Ediger, M. D.; Angell, C. A.; Nagel, S. R. *J. Phys. Chem.* **1996**, *100*, 13200–13212.
- (52) Debenedetti, P. G.; Stillinger, F. H. *Nature* **2001**, *410*, 259–267.
- (53) Xu, W.; Cooper, E. I.; Angell, C. A. *J. Phys. Chem. B* **2003**, *107*, 6170–6178.
- (54) (a) Tokuda, H.; Hayamizu, K.; Ishii, K.; Abu, M. S.; Watanabe, M. *J. Phys. Chem. B* **2004**, *108*, 16593–16600. (b) Tokuda, H.; Tsuzuki, S.; Susan, M. A. B. H.; Hayamizu, K.; Watanabe, M. *J. Phys. Chem. B* **2006**, *110*, 19593–19600.
- (55) Pregosin, P. *Prog. Nucl. Magn. Reson. Spectrosc.* **2006**, *49*, 261–288.
- (56) (a) Köddermann, T.; Wertz, C.; Heintz, A.; Ludwig, R. *ChemPhysChem* **2006**, *7*, 1944–1949. (b) Fumino, K.; Wulf, A.; Ludwig, R. *Angew. Chem., Int. Ed.* **2008**, *47*, 8731–8734.
- (57) Earle, M. J.; Esperança, J. M. S. S.; Gilea, M. A.; Canongia Lopes, J. N.; Rebelo, L. P. N.; Magee, J. W.; Seddon, K. R.; Widegren, J. A. *Nature* **2006**, *439*, 831–834.
- (58) Xiao, D.; Rajian, J. R.; Cady, A.; Li, S.; Bartsch, R. A.; Quitevis, E. L. *J. Phys. Chem. B* **2007**, *111*, 4669–4677.
- (59) Hansen, J.-P.; McDonald, I. R. *Theory of Simple Liquids*, 3rd ed.; Academic Press: London, 2006.
- (60) (a) Schmidt-Rohr, K.; Spiess, H. *Phys. Rev. Lett.* **1991**, *66*, 3020–3023. (b) Ediger, M. D. *Annu. Rev. Phys. Chem.* **2000**, *51*, 99–128. (c) Hedges, L. O.; Jack, R. L.; Garraghan, J. P.; Chandler, D. *Science* **2009**, *323*, 1309–1313.
- (61) (a) Shannon, R. D. *Acta Crystallogr.* **1976**, *A32*, 751–767. (b) Huheey, J. E.; Keiter, E. A.; Keiter, R. L. *Inorganic Chemistry: Principles of Structure and Reactivity*, 4th ed.; Harper Collins College Publishers: New York, NY, 1993.